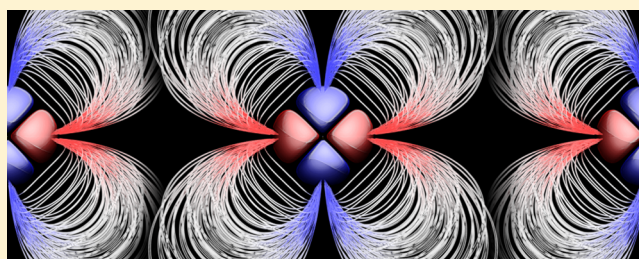# Multipolar Ewald Methods, 2: Applications Using a Quantum Mechanical Force Field

Timothy J. Giese, Maria T. Panteva, Haoyuan Chen, and Darrin M. York*

Center for Integrative Proteomics Research, BioMaPS Institute for Quantitative Biology and Department of Chemistry and Chemical Biology, Rutgers University, Piscataway, New Jersey 08854-8087, United States

S *Supporting Information*

ABSTRACT: A fully quantum mechanical force field (QMFF) based on a modified "divide-and-conquer" (mDC) framework is applied to a series of molecular simulation applications, using a generalized Particle Mesh Ewald method extended to multipolar charge densities. Simulation results are presented for three example applications: liquid water, *p*-nitrophenylphosphate reactivity in solution, and crystalline *N,N*-dimethylglycine. Simulations of liquid water using a parametrized mDC model are compared to TIP3P and TIP4P/Ew water models and experiment. The mDC model is shown to be superior for cluster binding energies and generally comparable for bulk properties. Examination of the dissociative pathway for dephosphorylation of *p*-nitrophenylphosphate shows that the mDC method evaluated with the DFTB3/3OB and DFTB3/OPhyd semiempirical models bracket the experimental barrier, whereas DFTB2 and AM1/d-PhoT QM/MM simulations exhibit deficiencies in the barriers, the latter for which is related, in part, to the anomalous underestimation of the *p*-nitrophenylate leaving group pK_a. Simulations of crystalline *N,N*-dimethylglycine are performed and the overall structure and atomic fluctuations are compared with the experiment and the general AMBER force field (GAFF). The QMFF, which was not parametrized for this application, was shown to be in better agreement with crystallographic data than GAFF. Our simulations highlight some of the application areas that may benefit from using new QMFFs, and they demonstrate progress toward the development of accurate QMFFs using the recently developed mDC framework.

1. INTRODUCTION

Molecular simulations provide atomic-level insight into a wide range of complex chemical processes, many of which benefit from—if not outright require—a fully quantum mechanical (QM) description. There has been considerable interest and effort made toward the development of linear-scaling quantum mechanical force fields (QMFFs) for molecular simulations.[1,2] QMFFs achieve their speed through a partitioning of the energy, whereby localized fragments are treated using traditional QM methods, such as density-functional[3] or semiempirical[4] models, and the interactions between the fragments are approximated by classical electrostatics and empirical potentials. In some QMFFs, such as the modified "divide-and-conquer" (mDC) method,[5] the electrostatic interactions between the fragments occur through atomic multipole expansions. Methods that generalize the linear-scaling evaluation of long-ranged electrostatic interactions to multipolar charge densities must be available and integrated into QMFF frameworks to be able to broadly test them within molecular simulations.[6]

In the first part of this series,[7] we described a multipolar Particle Mesh Ewald (PME) method that makes condensed phase mDC simulations tractable. In the second part, which is presented here, we explore a series of molecular simulation applications demonstrating the mDC framework using a

preliminary parametrization of the nonbond interaction model.[8] The first demonstration involves simulations of liquid water and the properties of small water clusters. The mDC binding energies and geometries of water clusters and the properties of bulk water are compared to the TIP3P and TIP4P/Ew water models, high-level QM benchmark data, and experimental measurements, where available. The second demonstration involves the study of the dissociative pathway for dephosphorylation of *p*-nitrophenylphosphate. The mDC barrier height and transition-state structure are compared with combined quantum mechanical/molecular mechanical (QM/MM) simulations performed with the DFTB2 and AM1/d-PhoT semiempirical models. The third demonstration involves simulation of crystalline *N,N*-dimethylglycine, and comparisons are made to experiment[9] and the general AMBER force field (GAFF).[10] These applications highlight areas that may benefit from using a QMFF and further serve to demonstrate considerable progress toward their use in molecular dynamics (MD) simulations.

2. METHODS

2.1. The mDC Quantum Force Field. The mDC method presented in ref 8 is a fully variational algorithm that is conceptually similar to the embedded X-Pol model pioneered by Gao,[4,11−14] but differs in the quantum methods used, the treatment of electrostatic interactions, and other technical details involving the interfragment interaction potential. The underlying goal of fragment-based linear-scaling methods, such as mDC and X-Pol, is to formulate a quantum model that is sufficiently fast to be routinely applied to condensed-phase environments. To achieve this speed, linear-scaling algorithms are used to compute the Fock matrix and to construct orthonormal molecular orbitals (MOs). Fragment-based quantum methods distinguish themselves from traditional QM models by avoiding the construction of *globally* orthonormal MOs via diagonalization of a matrix whose size is proportional to the entire system. Instead, mDC and other closely related QMFFs approximate the wave function using a Hartree product of antisymmetrized determinants of molecular fragments.[15] In other words, the system is divided into fragments or molecules, each of which is treated quantum mechanically using a basis of atomic orbitals (AOs) for the construction of MOs that are presumed to not overlap with the MOs of any other fragment. Because the MOs are taken to be a linear combination of AOs, this presumption also extends to AOs, so that the Fock or Kohn−Sham and overlap matrices become block diagonal in their AO representation. The solution of the system's MOs from the Roothaan or Kohn−Sham equations consequently simplifies to the diagonalization of a block-diagonal matrix, which reduces the computational complexity of this operation from $O(N^3)$ to $O(NK^3)$, where K is the number of AOs within a fragment. The above approximations appear, relative to a standard QM method, as an artificial lowering of the number of MO constraints, because the MOs of different fragments are now only presumed to not overlap, as opposed to having been enforced with Lagrange multipliers. When the molecules are separated by small distances, such that their AOs would be expected to significantly overlap, the lack of interfragment MO overlap constraints fails to produce an associated increase in the electronic energy, which must be modeled through some other means to recapture the effect. For example, other fragment models have used perturbative corrections,[16−18] valence bond theory,[19] or empirical models,[5,8,12,13] such as Lennard-Jones (LJ) or Buckingham potentials. The present work adopts the strategy of using standard pairwise LJ potentials to empirically account for the short-ranged repulsions described above, in addition to providing a treatment for London dispersion forces.

Although the fragments are not directly coupled through MO overlap, they remain coupled via the interaction of their densities. From this viewpoint, the fragments are embedded within an effective chemical potential arising from the other fragments. The mDC total energy is

$$E_{\text{mDC}} = \sum_A E_A(\mathbf{R}_A, N_A, \mathbf{p}_A) + E_{\text{inter}}(\mathbf{R}, \mathbf{q}) \tag{1}$$

where E_A is the *ab initio* electronic energy of fragment A with N_A electrons and atom positions $\mathbf{R}_A$ subjected to the external potential $\mathbf{p}_a = \partial E_{\text{inter}}(\mathbf{R},\mathbf{q})/\partial \mathbf{q}_a$. The DFTB3/3OB semi-empirical model[20] is used in the present work to compute E_A, unless noted otherwise. The interfragment interaction energy E_{inter} depends on the atomic positions and atomic multipole moments

$$q_{a,l\mu} = Z_a \delta_{l0}\delta_{\mu 0} - \int \rho_a(\mathbf{r}) C_{l\mu}(r - \mathbf{R}_a)\, d^3r \tag{2}$$

which are determined from the nuclear charge Z_a and the atom-partitioned electron density $\rho_a(\mathbf{r})$. The partitioning of the electron density to atomic centers is a choice, and our choice is to relate the density to the AO basis functions $\chi_i(\mathbf{r})$ and AO basis single-particle density matrix $\mathbf{P}$ in a manner analogous to Mulliken partitioning

$$\rho_a(\mathbf{r}) = \sum_{ij \in a} P_{ij}\chi_i(\mathbf{r})\chi_j(\mathbf{r}) + \sum_{b \neq a} f_{ab}(b_{ab}) \sum_{\substack{i \in a \\ j \in b}} P_{ij}\chi_i(\mathbf{r})\chi_j(\mathbf{r}) \tag{3}$$

$$b_{ab} = 2 \sum_{\substack{i \in a \\ j \in b}} P_{ij}S_{ij} \tag{4}$$

is a Mulliken bond-order, $\mathbf{S}$ is the AO overlap matrix, and $f_{ab}(b_{ab})$ is a smooth switching function that allows us to bias the partition between atom pairs to improve molecular electrostatic potentials.[8] For the water model described in the next section, a standard Mulliken partitioning is used between H and O $[f_{ab}(b_{ab}) = 1/2]$, whereas the parameters used to partition the density between other elements (C, N, P) are provided in ref 8. The working expression for the multipole moments is derived by inserting eq 3 into eq 2 while limiting the expansion of the two-center densities to charges

$$q_{a,l\mu} = \begin{cases} Z_a - \dfrac{b_{aa}}{2} - \displaystyle\sum_{\substack{b \in A \\ b \neq a}} f_{ab}(b_{ab})b_{ab} & \text{if } l = 0 \\[2em] \displaystyle\sum_{ij \in a} P_{ij}M_{ij}^{(l)} \sqrt{\dfrac{4\pi}{2l+1}} \int Y_{l\mu}(\Omega) Y_{l_i\mu_i}(\Omega) Y_{l_j\mu_j}(\Omega)\, d\Omega \\[1em] \quad \text{if } l > 0 \end{cases} \tag{5}$$

where

$$M_{ij}^{(l)} = \int_0^\infty \chi_i(r)\chi_j(r) r^{2+l}\, dr \tag{6}$$

are radial integrals that are treated as parameters to control the magnitude of the multipolar contribution arising from the single-center AO products. The two-center components of the density could be expanded to higher-order multipoles without undue computational effort, but we have not yet found their inclusion to be essential. When the electrostatics are limited to charges, the largest errors in DFTB3's molecular electrostatic potentials occur for sp^3 oxygen and sulfur lone-pairs, nitrogen lone-pairs, and sp and sp^2 carbons.[8,21] The one-center AO products' description of the atom hybridizations provides enough information to empirically improve upon these deficiencies with the parameters shown in eq 6.

The intermolecular interaction energy,

$$E_{\text{inter}}(\mathbf{R}, \mathbf{q}) = E_{\text{elec}}(\mathbf{R}, \mathbf{q}) + E_{\text{tail}} + \sum_{\substack{a > b \\ R_{ab} < R_{\text{cut}}}}' S_{\text{off}}(R_{ab})E_{\text{LJ},ab}(R_{ab}) \tag{7}$$

consists of the Coulomb interaction between the point multipoles using the multipolar PME method described in Part 1[7] and standard LJ interactions,

$$E_{LJ,ab}(R_{ab}) = \varepsilon_{ab}\left[\left(\frac{R_{min,ab}}{R_{ab}}\right)^{12} - 2\left(\frac{R_{min,ab}}{R_{ab}}\right)^{6}\right] \tag{8}$$

between atoms not within the same molecule. To ensure smooth atomic forces, the LJ interactions are switched off:

$$S_{off}(R_{ab}) = \begin{cases} 0 & \text{if } R_{ab} > R_{cut} \\ 1 & \text{if } R_{ab} < R_{sw} \\ 10u^3 - 15u^4 + 6u^5 & \text{otherwise} \end{cases} \tag{9}$$

where $u = (R_{cut} - R_{ab})/(R_{cut} - R_{sw})$, and a long-range tail correction is smoothly switched on:

$$E_{tail} = \sum_{\alpha,\beta}^{N_{types}} -\frac{2\pi N_\alpha N_\beta}{V}\left(\int_{R_{cut}}^{\infty} \frac{C_{6,\alpha\beta}}{R^6} R^2\, dR \right.$$
$$\left. + \int_{R_{sw}}^{R_{cut}} [1 - S_{off}(R)]\frac{C_{6,\alpha\beta}}{R^6} R^2\, dR\right) \tag{10}$$

The σ-spin Fock matrix of fragment A,

$$F_{ij,A}^\sigma = \frac{\partial E_A}{\partial P_{ij}^\sigma}\bigg|_R + \sum_{\substack{a \in A \\ l\mu \in a}} \frac{\partial E_{inter}}{\partial q_{a,l\mu}}\bigg|_R \frac{\partial q_{a,l\mu}}{\partial P_{ij}^\sigma}\bigg|_R \tag{11}$$

is obtained from elementary differentiation of the energy. Upon reaching a global self-consistency, the nuclear gradients of atom a in fragment A are

$$\frac{\partial E_{mDC}}{\partial X_a}\bigg|_{P,q} = \frac{\partial E_A}{\partial X_a}\bigg|_P + \frac{\partial E_{inter}}{\partial X_a}\bigg|_{P,q} - \sum_{ij \in A} Q_{ij,A}\frac{dS_{ij,A}}{dX_a} \tag{12}$$

where

$$Q_{ij,A} = \sum_{\sigma \in (\alpha,\beta)} \sum_k n_{k,A}^\sigma E_{kk,A}^\sigma C_{ik,A}^\sigma C_{jk,A}^\sigma \tag{13}$$

and $\mathbf{n}^\sigma$, $\mathbf{E}^\sigma$, and $\mathbf{C}^\sigma$ are the spin-resolved MO occupation numbers, eigenvalues, and eigenvectors, respectively.

In summary, the self-consistent field (SCF) procedure is as follows:

(1) Compute the spin-resolved density matrix $P_{ij,A}^\sigma = \sum_k n_{k,A}^\sigma C_{ik,A}^\sigma C_{jk,A}^\sigma$ and total density matrix $P_{ij,A} = P_{ij,A}^\alpha + P_{ij,A}^\beta$ of each fragment from their spin-resolved trial MO coefficients $\mathbf{C}_A^\sigma$.

(2) Evaluate the atomic multipole moments $\mathbf{q}_a$ from the density matrices (see eqs 5 and 6).

(3) Compute the interfragment electrostatic interaction energy and corresponding multipolar potentials $\mathbf{p}_a$ from the PME method described in Part 1 of this series.[7]

(4) Evaluate the DFTB3 energy (E_A) and Fock matrices ($\mathbf{F}_A^\sigma$) of each fragment from the density matrices $\mathbf{P}_A^\sigma$, and apply the external potential contribution to the Fock matrices (see eq 11).

(5) If the SCF has not converged, construct a new set of MO coefficients for each fragment and go back to step (1).

The LJ interactions can be computed before entering the SCF procedure or after the SCF has been completed.

2.2. Water Model and Simulations. The LJ parameters R_{min} and ε of O and H and the $M_{sp}^{(1)}$ and $M_{pp}^{(2)}$ multipole moment parameters of oxygen (see Table 1) were adjusted to simultaneously reproduce the geometries and binding energies

Table 1. Water Model Parameters

	mDC	3P	4P
R_{OH} (Å)	0.9571	0.9572	0.9572
R_{OM} (Å)			0.125
$\angle_{HOH}$ (deg)	110.48	104.52	104.52
q_H (a.u.)	[0.36155]	0.417	0.52422
ε_{OO} (a.u.)	3.096×10^{-4}	2.422×10^{-4}	2.594×10^{-4}
$R_{min,OO}$ (a.u.)	6.669	6.683	6.712
ε_{HH} (a.u.)	9.500×10^{-7}		
$R_{min,HH}$ (a.u.)	2.800		
$M_{sp}^{(1)}$ (a.u.)	−0.08		
$M_{pp}^{(2)}$ (a.u.)	2.4		

Table 2. Water Cluster Binding Energy and Geometry Statistics[a]

	ΔE (kcal/mol)		coordinate root-mean-square displacement, crms (Å)
	mean signed error, mse	mean unsigned error, mue	
mDC	0.32	0.54	0.15
3P	−1.81	2.17	0.44
4P	−5.59	5.59	0.32

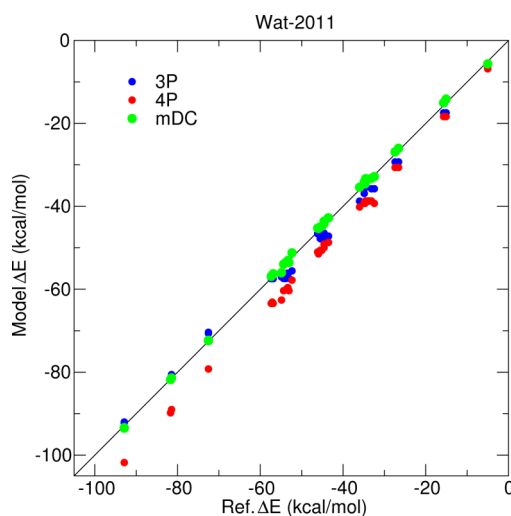[a]Reference values taken from ref 24.

Figure 1. Water cluster binding energies. Reference values taken from ref 24.

of small water clusters (Table 2 and Figure 1) and the condensed phase properties of water (Table 3) using a single set of parameters. The parametrized mDC model is compared to the standard TIP3P[22] and TIP4P/Ew[23] water models, denoted by 3P and 4P in the tables and figures.

Table 2 and Figure 1 compare the binding energies ΔE of geometry optimized gas-phase water clusters [$(H_2O)_n$ for $n = 2-10$] computed with mDC, TIP3P, and TIP4P/Ew to the *ab initio* results taken from ref 24 (RI-MP2/CBS with a CCSD(T)/aug-cc-pVDZ correction). The coordinate root-mean-square displacement (crms) is an all-atom comparison of the geometry optimized model and reference structures. The internal geometry of the mDC water was not constrained during the optimization of cluster geometries, which is consistent with the procedure used to generate the reference data. The MM water models are inherently rigid because they

Table 3. Properties of Liquid Water

T (K)	Density, ρ (g cm⁻³)				Heat Capacity, c_p (cal mol⁻¹ K⁻¹)				κ_T (× 10⁻⁶ bar⁻¹)			
	expt[a]	mDC	3P	4P	expt[b]	mDC	3P	4P	expt[a]	mDC	3P	4P
263	0.9981	0.9971	1.0134	0.9988		21.9	17.5	20.4	56	63	51	50
273	0.9998	0.9995	1.0061	0.9996	18.2	22.9	17.2	20.4	51	57	52	46
285	0.9995	0.9996	0.9971	0.9985	18.1	21.5	16.8	19.5	47	54	54	47
298	0.9970	0.9969	0.9856	0.9951	18.0	21.8	17.4	19.0	45	49	57	47
310	0.9933	0.9920	0.9752	0.9908	18.0	20.5	16.7	19.1	44	50	58	47
323	0.9880	0.9853	0.9628	0.9842	18.0	21.6	17.0	18.8	44	50	63	49
335	0.9822	0.9775	0.9508	0.9771	18.0	20.9	17.4	18.9	45	51	68	50
348	0.9748	0.9674	0.9370	0.9687	18.1	19.4	17.0	19.0	46	53	72	53
373	0.9584	0.9445	0.9077	0.9491	18.2	19.4	17.6	18.3	49	58	90	59

T (K)	ΔH_{vap} (kcal mol⁻¹)				$\Delta H'_{vap}$ (kcal mol⁻¹)			
	expt[b]	mDC	3P	4P	expt[b]	mDC	3P	4P
263		11.19	9.39	11.15		11.04	9.24	11.00
273	10.77	11.02	9.28	11.01	10.77	10.90	9.15	10.88
285	10.65	10.83	9.14	10.83	10.65	10.73	9.05	10.74
298	10.51	10.62	9.00	10.66	10.51	10.56	8.93	10.59
310	10.39	10.44	8.87	10.50	10.39	10.40	8.82	10.45
323	10.26	10.25	8.72	10.33	10.26	10.22	8.70	10.30
335	10.13	10.07	8.59	10.18	10.13	10.06	8.59	10.17
348	9.99	9.89	8.45	10.02	9.99	9.89	8.46	10.02
373	9.72	9.52	8.18	9.71	9.72	9.55	8.21	9.74

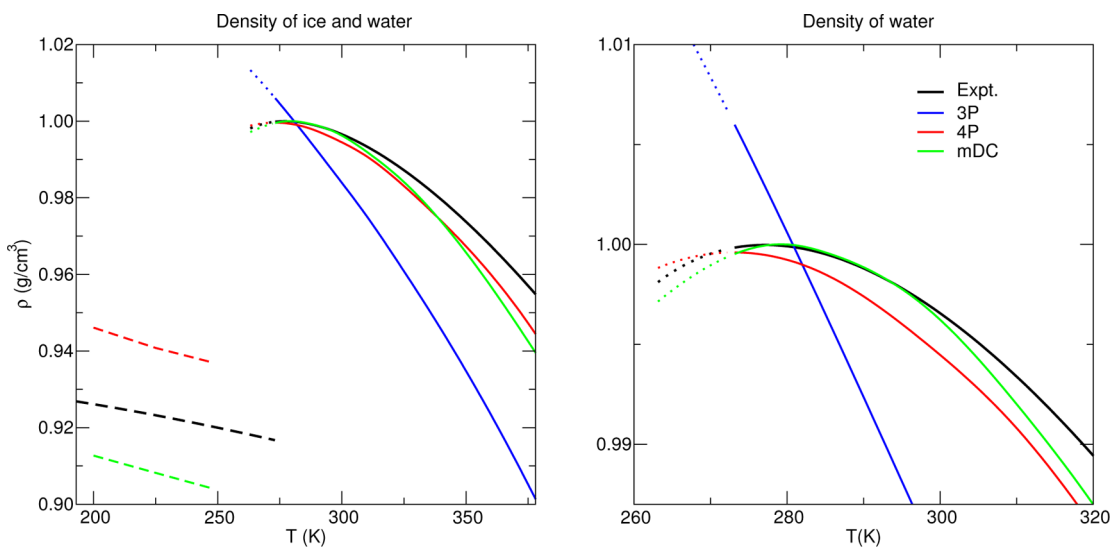[a]Data taken from ref 79. [b]Data taken from ref 80.

Figure 2. Density of ice (I_h (dashed line (- - -)), supercooled water (dotted line (···)), and liquid water (solid line (—)). Experimental values taken from refs 79 and51.

were designed to be used in condensed-phase environments only.

The condensed-phase water simulations used to generate Figures 2 and 3, the data shown in Table 3, and the dielectric constants appearing in Table 4 were performed on cubic boxes containing 512 waters simulated in the isothermal−isobaric ensemble at atmospheric pressure with a modified version of PMEMD.[25] The Andersen thermostat[26] (1 ps coupling constant) and Monte Carlo (MC) barostat[25] (0.1 ps per isotropic volume scaling attempt) were used to control the temperature and pressure of the system. Statistics were collected from 8 ns of sampling with a time step of 1 fs for all simulations except the liquid-phase TIP3P and TIP4P/Ew simulations, which were run for 25 ns. For all models, the LJ

interactions were explicitly computed within a 9 Å cutoff and supplemented with a tail correction to mimic the long-range interactions. Our implementation of the mDC model transitions between these two limits (see eqs 7−10) from 8 Å to 9 Å to pedantically guarantee that smooth gradients are rigorously enforced; however, the difference between smooth and precipitous transitions at 9 Å does not appear to effect our results beyond the statistical uncertainties engendered by the simulations' finite sampling. PME[27,28] and multipolar PME[7] electrostatics were performed with sixth-order Cardinal B-spline interpolation on a 1 pointt/Å regular grid. The SHAKE algorithm[29,30] is applied to all water models when performing condensed-phase simulations to avoid the use of excessively small time steps. SHAKE was chosen to constrain the mDC
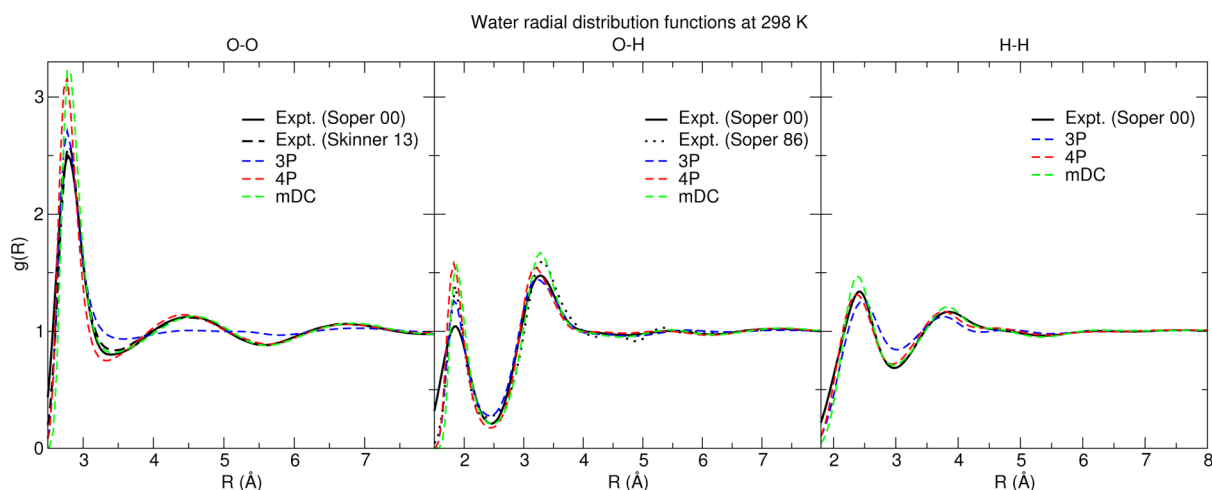
Figure 3. Water radial distribution functions. Experimental values taken from ref 83 (Soper 00), ref 84 (Skinner 13), and ref 85 (Soper 86).

Table 4. Water Diffusion Coefficient and Dielectric Constant at 298 K

	Water Diffusion Coefficient, D ($\times 10^{-5}$ cm^2 s^{-1})		
	Avg.	Extrap.	dielectric constant, ε
expt[a]	2.30	2.30	78
mDC	2.29	2.49	48
3P	5.49	6.32	99
4P	2.42	2.79	63

[a]Experimental diffusion taken from ref 81. Experimental dielectric taken from ref 82.

water to the DFTB3/3OB[20] gas-phase water structure, instead of the experimental gas phase structure. This choice was physically motivated by providing a definition for a zero of potential energy that avoids the need for applying monomer deformation energies when computing the interactions of water.

Several condensed-phase properties are computed[31] and compared with the experiment, including the heat of vaporization, the isothermal compressibility, the isobaric heat capacity, and the static dielectric constant:

Heat of Vaporization:

$$\Delta H_{vap} = k\langle T \rangle - \frac{\langle U_{pot} \rangle + p\langle V \rangle}{N} - E_{pol} \tag{14}$$

or

$$\Delta H'_{vap} = \Delta H_{vap} + C_{ni}(T) + C_{vib}(T) \tag{15}$$

Isothermal Compressibility:

$$\kappa_T = \frac{\langle V^2 \rangle - \langle V \rangle^2}{k\langle T \rangle \langle V \rangle} \tag{16}$$

Isobaric Heat Capacity:

$$c_p = \frac{\langle H^2 \rangle - \langle H \rangle^2}{k\langle T \rangle \langle V \rangle} + \frac{\partial E_{vib}(T)}{\partial T} \tag{17}$$

Static Dielectric Constant:

$$\varepsilon = 1 + 4\pi \frac{\langle \boldsymbol{\mu}^T \cdot \boldsymbol{\mu} \rangle - \langle \boldsymbol{\mu} \rangle^T \cdot \langle \boldsymbol{\mu} \rangle}{3k\langle T \rangle \langle V \rangle} \tag{18}$$

where brackets indicate time-averaged quantities from the generated ensemble, U_{pot} is the total potential energy of the system, V is the volume of the simulation box, H is the enthalpy ($H = U_{pot} + E_{kin} + pV$), $\boldsymbol{\mu}$ is the dipole moment of the system, and E_{pol} is an *ad hoc* correction applied to the nonpolarizable water models ($E_{pol} = \Delta\mu_{wat}^2/2\alpha$) to account for the condensed-phase water's increased self-energy associated with having used an enhanced dipole moment, relative to the experimental gas-phase dipole moment ($\Delta\mu_{wat}$). Upon inserting the model and experimental dipole moment and the experimental gas phase polarizability, the E_{pol} corrections for TIP3P and TIP4P/Ew are 1.18 and 1.05 kcal/mol, respectively. The E_{pol} correction is not applied to the mDC model, because of its explicit treatment of polarization within $\langle U_{pot} \rangle$. $C_{ni}(T)$, $C_{vib}(T)$, and $\partial E_{vib}(T)/\partial T$ are *ad hoc* corrections introduced by Horn[23] that account for the nonideality of the water vapor, the difference between the vacuum and liquid-phase vibrational energies, and the vibrational energy contribution to the heat capacity, respectively. These quantities are provided for several temperatures in Table 4 of ref 23. We computed the corrections by spline interpolation of Horn's pretabulated values at our simulation temperatures. The ΔH_{vap} comparisons in Table 3 are made with (using eq 15) and without (using eq 14) these corrections for all models.

Table 4 and Figure 4 compare the self-diffusion coefficients of water at 298 K. The diffusion coefficients were computed from canonical ensemble simulations, similar to the protocol performed by others,[32,33] using a series of system sizes (512, 768, 1024, and 1280 waters) at equilibrated system densities. Each simulation was run for 1.2 ns using the Berendsen weak coupling scheme to control the temperature.[34] The diffusion constant was computed from numerical differentiation of the Einstein relation:

$$D = \frac{1}{6} \frac{d}{d\tau} \frac{1}{N_{wat}} \sum_i^{N_{wat}} \langle |\mathbf{R}_i(t + \tau) - \mathbf{R}_i(t)|^2 \rangle_t \tag{19}$$

In other words, the water-averaged autocorrelation of the mean-squared displacement of the oxygen position was computed for a series of time lags, and a linear regression was used to determine the slope of the resulting line.

The self-diffusion coefficient is known to exhibit a dependence on system size that is almost linear with the reciprocal length of the simulation box (see Figure 4).[35,36] The values
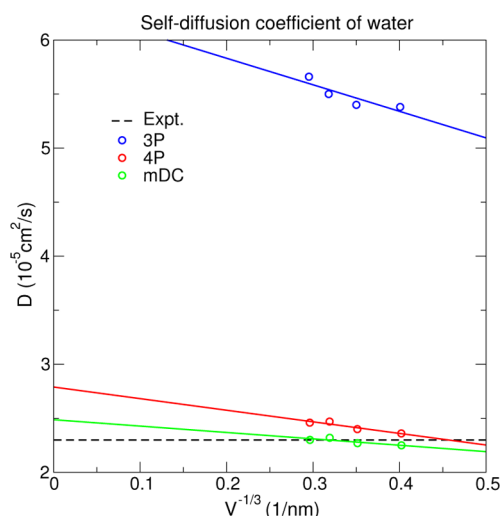
Figure 4. Box size dependence on the self-diffusion coefficient of water at 298 K. Experimental value taken from ref 81.

"Avg." and "Extrap." in Table 4 are the average of the four diffusion coefficients and the diffusion constant extrapolated to infinite box size from linear regression, respectively.

Figure 2 compares the experimental density of ice (I_h) to mDC and TIP4P/Ew simulations at 200, 225, and 248 K. For clarity, the properties of ice were not considered during the parametrization of either model. The ice simulations were performed in a manner analogous to those described above for the liquid phase, which we will not fully repeat here. The ice I_h crystals are composed of 576 waters replicated from the unit cell to fill an orthorhombic simulation box. The crystals were equilibrated for 2 ns in the isothermal−isobaric ensemble with anisotropic volume changes to relax the lattice vectors. The reported densities are simulation averages from 8 ns of production in the isothermal−isobaric ensemble. Figure 2 does not display the density of TIP3P, because it has a very low melting point.[37]

2.3. p-Nitrophenyl Phosphate Reaction. Figure 5 compares the free-energy profiles of the p-nitrophenyl phosphate (pNPP) dissociative reaction in solution using semiempirical QM/MM and mDC models. The simulations were performed in the isothermal−isobaric ensemble at 298 K within a box of 1550 waters, following a protocol that is analogous to the water simulations described in the previous section. The reaction profile was generated from a series of 56 umbrella window simulations that force the separation between the phosphorus and oxygen depicted in Figure 5, using a harmonic restraining potential with a force constant of 75 kcal mol^{-1} Å^{-2}. Each window was equilibrated for 300 ps and another 300 ps was simulated for production. The value of the reaction coordinate was printed every 20 steps, which was then analyzed using the variational free-energy profile (vFEP) method[38] to produce the profiles displayed in Figure 5. The QM/MM simulations were performed with TIP3P water in combination with the DFTB2/MIO[39−41] or AM1/d-PhoT[42] semiempirical models, which were readily available for use in SANDER.[25] The mDC simulations were performed twice: the "mDC/3OB" profile employed the 3OB parametrization of DFTB3,[20] whereas "mDC/OPhyd" made use of the DFTB3/3OB model supplemented with a modified O−P repulsive potential designed to improve phosphate hydrolysis reaction energies.[43] The mDC electrostatic and LJ parameters of the solute atoms were taken from ref 8. The standard GAFF LJ parameters were used in the QM/MM simulations.

2.4. N,N-Dimethylglycine Crystal Simulations. Table 5 compares experimental[9] isotropic and anisotropic heavy-atom displacement parameters of crystalline N,N-dimethylglycine (DMG) as a function of temperature to those obtained from GAFF and mDC simulations. The crystal lattice was constructed from the experimentally determined asymmetric unit of the orthorhombic polymorph,[9] which consists of two DMG molecules. The fundamental unit cell of the crystal contains 16 DMG molecules that are related to the asymmetric unit by fundamental symmetry operations. A supercell composed of 18 unit cells (288 DMG molecules), shown in Figure 6, was then constructed from elementary translations of the unit cell along the lattice vectors. The crystal supercell was simulated at each temperature in the canonical ensemble using the experimental density for 325 ps, the first 25 ps of which was discarded as equilibration, and a trajectory of 1200 frames of production was stored for analysis. The 18 unit cells within
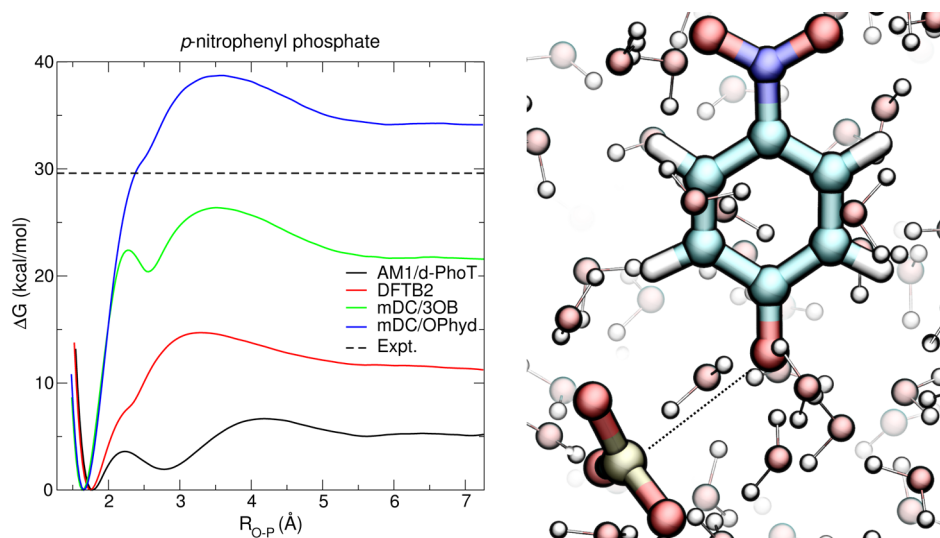

Figure 5. p-nitrophenol phosphate. Experimental value taken from ref 65.

Table 5. Pearson Correlation and Mean Unsigned Errors of the Heavy-Atom Isotropic and Anisotropic Displacement Parameters in N,N-Dimethylglycine, Relative to the Experiment (See Ref 9)

	Pearson Correlation, R		Mean Unsigned Error, mue (Å^2)	
T (K)	GAFF	mDC	GAFF	mDC
Isotropic Displacement Parameters				
225	0.79	0.93	0.0466	0.0126
250	0.88	0.94	0.0724	0.0168
275	0.88	0.95	0.0521	0.0234
295	0.90	0.94	0.0529	0.0328
Anisotropic Displacement Parameters				
225	0.76	0.89	0.0550	0.0153
250	0.79	0.91	0.0860	0.0169
275	0.83	0.92	0.0520	0.0199
295	0.85	0.93	0.0492	0.0231

each frame of the trajectory were translated to a common center to produce 21600 frames of a 16-molecule unit cell. Similarly, the reverse operations that relate the unit cell to the asymmetric unit were applied to produce 172 800 frames of the two-molecule asymmetric unit (see Figure 6). The 3×3 covariance matrix of each heavy-atom position, which can be defined as

$$U_{XY,a} = \langle (X_a - \langle X_a \rangle)(Y_a - \langle Y_a \rangle) \rangle \tag{20}$$

is diagonalized to produce three eigenvalues ($u_{1,a}$, $u_{2,a}$, $u_{3,a}$), whose average value and standard deviation are taken to be the isotropic and anisotropic "displacement parameters", respectively.

Average Value:

$$u_{\text{iso},a} = \frac{\sum_i^3 u_{i,a}}{3} \tag{21}$$

Standard Deviation:

$$u_{\text{aniso},a} = \sqrt{\frac{\sum_i^3 (u_{i,a} - u_{\text{iso},a})^2}{3}} \tag{22}$$

The values of $u_{\text{iso},a}$ and $u_{\text{aniso},a}$ of each heavy element are compared to those reported from the analysis of experimental diffraction data, and the statistics arising from these comparisons are shown in Table 5.

3. RESULTS AND DISCUSSION

3.1. mDC Water Model. Simple MM models, such as TIP4P/Ew, are capable of adequately modeling the condensed-phase properties of water for most applications; however, the
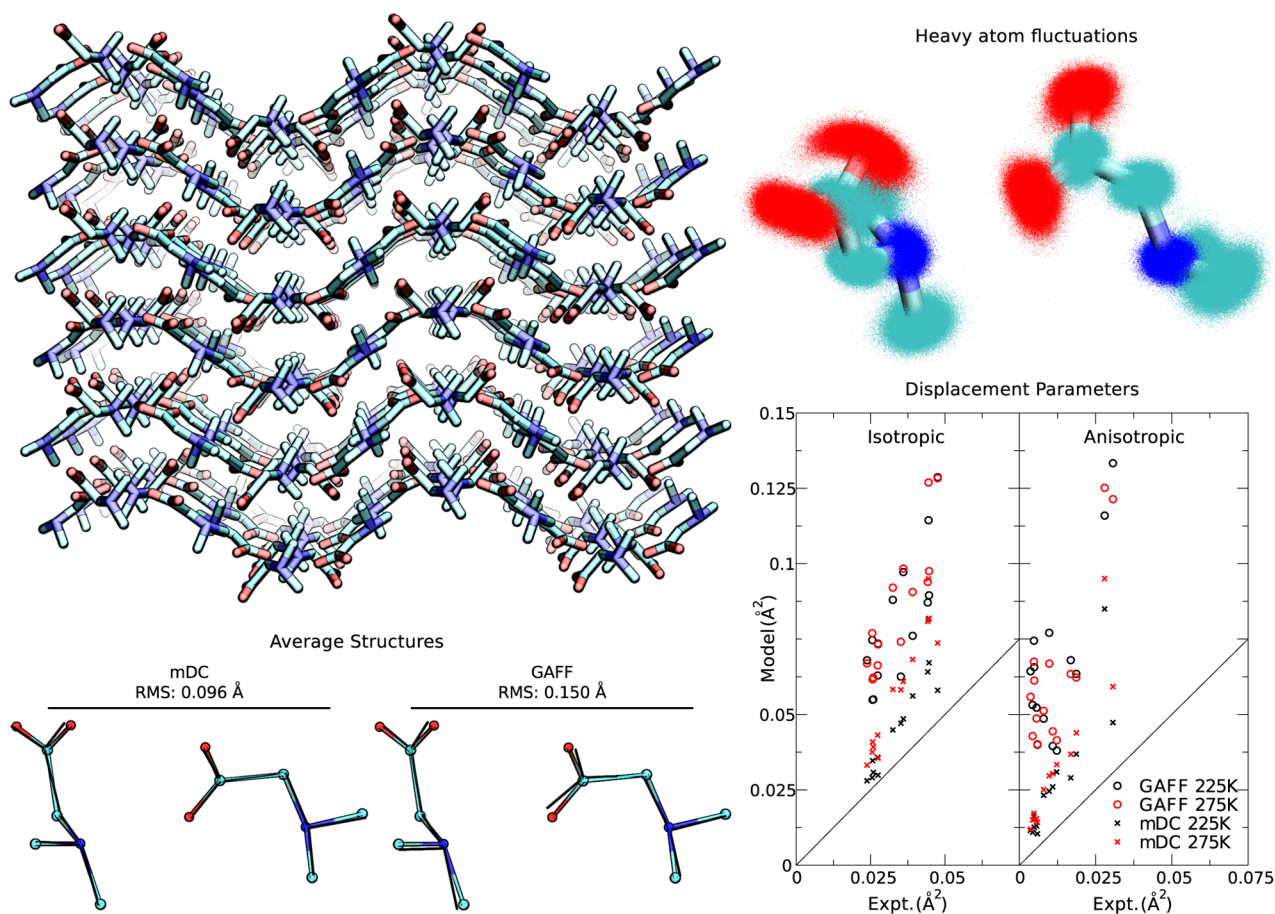

Figure 6. N,N-dimethylglycine crystal lattice used in the MD simulations. The experimentally observed asymmetric unit was taken from ref 9. The mDC and GAFF ensemble averaged asymmetric unit structures (black lines) at 225 K are overlaid on the experimental coordinates (colored molecules). The mDC heavy atom fluctuations at 225 K are shown by overlaying the entire ensemble of structures on the experimental coordinates. The display of so many structures causes them to appear as "fuzzy clouds". (Inset shows the correlation between experimental and calculated heavy atom isotropic and anisotropic displacement parameters. Each data point corresponds to one heavy atom in the asymmetric unit.)

limitations of simple models often mean that this type of targeted parametrization limit their ability to simultaneously reproduce *ab initio* intermolecular interaction energies within small molecule clusters. The strategy used to develop the parameters listed in Table 1, therefore, was to choose a large set of trial parameters that each reproduced the *ab initio* water binding energies (see Table 2 and Figure 1) to within a mean unsigned error (mue) of 1 kcal/mol, and then prune and refine the parameters based on the results of short condensed-phase simulations until the mDC condensed-phase properties were comparable to TIP4P/Ew results. Specifically, we chose the parameters to reproduce the location and height of the 3.4 and 4.6 Å peaks in the experimental O−O RDF at 298 K. Second, we rejected parameters if they did not reproduce the experimental densities at 273, 298, and 310 K well. Finally, the heat of vaporization (without Horn's $C_{ni}(T)$ and $C_{vib}(T)$ corrections[23]) were monitored at 298 K and compared with our TIP4P/Ew results. Considering that TIP4P/Ew is remarkably good model for condensed-phase properties, we rejected parameters that caused mDC to deviate from the ΔH_{vap} value of TIP4P/Ew by more than 0.1 kcal/mol. Automated procedures to aid parameter development, such as the ForceBalance method[44] used to develop iAMOEBA,[45] have been described in the literature,[46−49] but were not used here. During this process, we observed a very strong correlation between the mue values of the water cluster and the ΔH_{vap} value of the condensed phase. Furthermore, the RDFs (Figure 3) were found to be highly sensitive to the value of $R_{min,OO}$, and the water cluster hydrogen bond angles were sensitive to oxygen's $M_{pp}^{(2)}$ quadrupole parameter. As a result of this procedure, the mDC cluster mue's are 10 times smaller than TIP4P/Ew and the agreement with the *ab initio* geometries, as measured by the crms values, improve by a factor of 2.

The temperature dependence of the mDC water density (Figure 2) is comparable to TIP4P/Ew, and it exhibits a maximum near 279 K, which is similar to the experimental maximum of 277 K. The mDC and TIP4P/Ew simulations yield similar isothermal compressibilities and heats of vaporization, as shown in Table 3; however, the TIP4P/Ew heat capacity is closer than mDC to the reference value by 1−2 cal mol^{-1} K^{-1}. The TIP4P/Ew self-diffusion coefficient (Figure 4) is 5%−20% too high, depending on how it is measured, whereas the mDC water model is 0 to 8% too high. On the other hand, the experimental dielectric constant (Table 4) is better reproduced by TIP4P/Ew than mDC. The underestimation of the dielectric constant is indicative of either having a dipole moment that is too small, an orientational interaction that is overstabilizing (the quadrupole-charge interactions, for example), or some combination of the two. The mDC water molecule has a gas-phase dipole moment of 1.95 D, which is close to the experimental value of 1.85 D. However, the gas-phase polarizability of mDC water, being based on the minimal valence basis DFTB3 semiempirical model, is considerably underestimated, relative to *ab initio* calculations. It is possible that the quadrupolar interactions are slightly too strong and thereby mask the attraction that would be incurred from additional dipole polarization.

A comparison between mDC, TIP4P/Ew, and experimental ice I$_h$ densities is included in Figure 2. The mDC and TIP4P/ Ew densities are too low and too high, respectively, by approximately equal amounts; however, neither model was parametrized to reproduce solid-state properties. At 248 K, the density of mDC (0.904 g/cm^3) is in good agreement with the

literature value of TIP4P/Ice (0.909 g/cm^3).[50] We have not determined the melting point of mDC ice; however, we note that the enthalpy of mDC ice I$_h$ is 0.34 kcal/mol more stable than TIP4P/Ew for all 3 temperatures, and both models yield nearly identical supercooled liquid enthalpies at 263 K (Table 3). We are encouraged to see mDC's increased lattice stability in this comparison, because TIP4P/Ew's melting temperature is too low.[50] The comparison of calculated sublimation enthalpies to experimental measurements[51] would likely require a more rigorous treatment for nuclear quantum effects than what we have performed here.[52] With the exception of the *ad hoc* corrections for liquid water (eq 15), our calculated enthalpies assume that the intramolecular vibrational energy of water is unchanged by the condensed-phase environment, and our classical simulations of ice I$_h$ ignore the zero-point vibrational energy of the lattice. These assumptions are faulty at low temperatures[53] and they can also affect liquid water properties,[54,55] as is evident by comparing ΔH_{vap} to $\Delta H'_{vap}$ in Table 3. Previous comparisons between Path Integral and classical simulation methods suggest nuclear quantum phenomena can also subtly lower the density and increase the self-diffusion coefficient of liquid water at 298 K.[56,57]

The TIP3P and TIP4P/Ew water models achieve awesome performance on Graphics Processing Unit accelerated MD programs.[58,59] For example, AMBER's PMEMD CUDA program[60] can simulate a box of 512 waters using the protocol described in this manuscript at a rate of 100 ns/day on a NVIDIA GeForce GTX 765M. On an 8-core Intel Xeon workstation, the parallel Central Processing Unit implementation of PMEMD[25] achieves 22 ns/day, whereas mDC simulates 0.8 ns/day on the same computer. Our implementation of the brute force $O(N^3)$ variant of traditional DFTB3 has not been adapted for periodic boundary conditions; however, vacuum calculations of 512 waters on 8 cores produces only 10^{-4} ns/ day. A more detailed analysis of mDC's performance can be found in Part 1 of this series.[7]

Overall, the mDC simulations are able to model the structure and energetics of small clusters, relative to high-level *ab initio* calculations, considerably better than the empirical TIP3P and TIP4P/Ew models, while, at the same time, reproducing experimental condensed-phase properties generally better than TIP3P and similar to TIP4P/Ew. It is a considerably challenging problem in force field development to design robust models for water that can accurately reproduce both cluster and condensed-phase properties. The relative ease by which the mDC model achieved this result has important implications for simulations in heterogeneous environments where the local electrostatic environment can vary considerably. One could attribute mDC's transferability to its multipolar electrostatics and/or electronic polarization provided by the underlying QM Hamiltonian's MOs; however, care should be taken to not misrepresent mDC as being merely a multipolar, polarizable force field. In other words, our examination of water properties, by itself, does not well-characterize the breadth of benefits offered by QMFFs, because QM Hamiltonians are not really required to achieve high quality results for bulk water and water clusters. On the contrary, QMFFs offer the possibility to extend the scope of applications to include problems that require a detailed description of the electronic distribution and/ or MOs (chemical reactions and spectroscopy, for example) of large systems in which a localized "QM region" is either: ill-defined (molecular crystals and ionic liquids, for example), is sensitive to the QM/MM decomposition or potential, or when

well-established MM force field parameters are unavailable (nonstandard drug ligands, for example). Moreover, the efficiency of QMFFs afford the degree of configurational sampling required to make meaningful comparisons with experiment, and their nonbond interactions can be improved beyond the capabilities of the underlying QM Hamiltonian through the tuning of empirical parameters. Thus, we assert that MO-based QMFFs are arguably better described as being *extraordinarily fast and empirically accurate linear-scaling quantum methods* rather than *exotic, polarizable force fields*. Nevertheless, QMFF methodologies live in a "middle ground" between polarizable force fields and linear-scaling quantum methods and may appear to take on characteristics of each, depending on how they are applied.[61]

3.2. *p*-Nitrophenyl Phosphate Reaction. Relative to traditional MM force fields, QMFFs have the advantage in being capable to model processes where bond formation and cleavage occur. In this section, we examine the dissociative mechanism of dephosphorylation of *p*NPP in aqueous solution, which is a prototype phosphoryl transfer reaction,[62] as an example application. Unlike the water cluster and bulk liquid properties discussed in the previous section, no effort was made to tune the mDC LJ or electrostatic parameters specifically for this application.

The *p*NPP model system plays an important role in phosphoryl transfer reaction studies. The pK_a of *p*-nitrophenol (~7.2) is considerably lower than the native 5′-alkoxide leaving group in RNA cleavage transesterification. Therefore, *p*NPP is often used as an "enhanced" phosphoryl transfer leaving group to study linear free-energy relationships (LFERs)[63] and kinetic isotope effects (KIEs).[62,64] LFERs and KIEs are powerful experimental methods to infer catalytic mechanisms, because they report directly on the structure, bonding, and local charge of the transition state.

The barrier for this reaction in solution has been experimentally estimated to be 29.6 kcal/mol.[65] As a reference for further comparison, we performed optimizations for the reactant and transition-state geometries using B3LYP/6-31++G** coupled with the polarizable continuum implicit solvent model (PCM)[66,67] and UAKS radii.[68] The B3LYP calculations predict a barrier of 19.5 kcal/mol, which is 10 kcal/mol lower than experiment. The discrepancy is, to some extent, influenced by the error in the B3LYP proton affinity,[69] which is 4.2 kcal/mol lower than high-level reference calculations. Previous *ab initio* calculations have shown that the barrier for this reaction is very sensitive to microsolvation.[70] In particular, it was found that B3LYP/PCM calculations supplemented with 12 and 14 explicit water molecules increase the barrier to 21.1 and 29.3 kcal/mol, respectively[70]

The *p*NPP dephosphorylation dissociative mechanism free-energy profiles are shown in Figure 5. Generally, none of the calculated barriers compare well with the experiment. Nonetheless, the two mDC models bracket the experimental barrier and are more similar to it than any of the other models. The mDC/3OB and mDC/OPhyd models underpredict and overpredict the experimental barrier by 3.2 and 9.1 kcal/mol, respectively. The appearance of an artificial dip in the mDC/3OB profile at R_{O-P} = 2.5 Å is a symptom that we have encountered with DFTB3/3OB in other unpublished applications involving phosphorus chemistry. We hypothesize that this is produced from the increased stabilization of the *d*−*d* tight-binding diagonal matrix elements that were given to phosphorus in the DFTB3/3OB parameters, relative to

DFTB3/MIO;[71] however, a more-detailed analysis would be required to support this supposition. This feature is largely eliminated in the mDC/OPhyd profile.

The DFTB2 and AM1/d-PhoT QM/MM simulations produce barriers significantly lower than the experiment. The AM1/d-PhoT model was originally developed specifically for phosphoryl transfer reactions; however, its treatment of nitro groups is poor. For example, the AM1/d-PhoT proton affinity of *p*-nitrophenol is 12.7 kcal/mol lower than experiment. This effect is, to some extent, an amplified byproduct of a systematic error in the B3LYP proton affinity discussed above that served as the benchmark reference used during the AM1/d-PhoT parametrization.[42] We suggest that each methods' capacity to reproduce the experimental barrier depends on their ability to simultaneously model the P−O covalent bond strength and the electron-withdrawing power of the nitro group. Overall, although there is very considerable room for improvement in all of the simulations, the simulations with the mDC model perform considerably better than the QM/MM models considered here, as well as the B3LYP model with simple PCM-only solvation.

3.3. *N,N*-Dimethylglycine Crystal Simulations. Another application area that stands to benefit from periodic boundary simulations using QMFFs is the study of small-molecule crystals. Of particular pharmaceutical interest is the study of polymorphism in molecular crystals of drug compounds.[72−75] A great deal of effort is devoted to the understanding of polymorphism of pharmaceutical compounds, because different synthetic pathways can lead to different crystal polymorphs, which, in turn, have dramatically different bioavailability and biological activity. There has been much research effort and progress made in recent years in the study of the stability of organic crystals from molecular simulations, and, for these applications, many-body polarization effects have been demonstrated to be very important.[76−78] Here, we apply mDC to crystal simulations of *N,N*-dimethylglycine and make comparison to experiment and GAFF simulations.[10]

Figure 6 and Table 5 compare the structure and correlation of the experimentally observed isotropic and anisotropic displacement parameters to those obtained from GAFF and mDC simulations. A superposition of the average asymmetric unit structure from the crystal simulation with the crystal structure gives a root-mean-square (rms) displacement of 0.096 Å for mDC and 0.15 Å for GAFF. The average structures from both simulations thus are very close to the experimental structure, and the mDC result is particularly impressive. The Pearson correlation coefficients of the mDC displacement parameters are generally greater than 0.9, whereas the GAFF correlation coefficients range from 0.76 to 0.9. As displayed in Figure 6, both GAFF and mDC produce large errors in both the isotropic and anisotropic displacement parameters, even though their correlation to the experiment is reasonable. Nonetheless, the mDC errors are two or more times smaller than GAFF, as shown in Table 5. Overall, the mDC method, without having specifically tuned the parameters for this application, performs markedly better than GAFF.

4. CONCLUSION

In this work, we incorporated the recently developed multipolar PME method into the mDC linear-scaling quantum force field framework and applied it to condensed-phase simulations of water, the *p*-nitrophenylphosphate (*p*NPP) dissociation reaction free-energy profile, and the reproduction of the

experimental isotropic and anisotropic displacement parameters observed in crystalline *N,N*-dimethylglycine for several temperatures. An mDC water model was parametrized to simultaneously reproduce the interaction energies and geometries of small water clusters and the bulk properties of liquid water. The parametrized mDC water model is found to be comparable to the TIP4P/Ew at reproducing the bulk properties of water, including the density, heat of vaporization, isothermal compressibility, and diffusion coefficient; however, the static dielectric constant of mDC water was found to be too low, which may arise from the underpredicted polarizability inherent within DFTB3. On the other hand, the mDC model performs substantially better than TIP4P/Ew, for reproducing the high-level *ab initio* energetics of small water clusters, and significantly better, with respect to the geometries. The mDC model was applied to the *p*NPP dissociation reaction to demonstrate its ability to model chemical reactions in complex condensed-phase environments. At the same time, comparisons were made to two other widely available QM/MM methods. Although the barrier height of the mDC free-energy profile was substantially closer to the experiment than either DFTB2/TIP3P, AM1/d-PhoT/TIP3P, or B3LYP with PCM solvation, more effort must be made to further develop and test the DFTB3 model and mDC parameters to increase the predictive capability in applications to enzymes and ribozymes. The DMG crystal simulation was performed to highlight an application area that extends beyond simple solvation with water. The mDC displacement parameters were found to correlate better with the experiment than the general AMBER force field by as much as 15%, and the mean unsigned errors (mues), relative to the experiment, were reduced by a factor of 2. In summary, the results suggest that QMFFs developed within the mDC framework are both computationally tractable and robust, exceeding the accuracy of standard force fields and QM/MM models. Full development of new QMFFs promise to add new levels of accuracy and predictive capability to application areas involving chemical reactions and processes where inherent limitations in the form of standard force fields are a bottleneck to accuracy and predictive capability.

ASSOCIATED CONTENT

Ⓢ Supporting Information

The structures and energies of the water clusters appearing in Figure 1 are provided. This material is available free of charge via the Internet at http://pubs.acs.org/.

AUTHOR INFORMATION

Corresponding Author
*E-mail: york@biomaps.rutgers.edu.

Notes
The authors declare no competing financial interest.

ACKNOWLEDGMENTS

REFERENCES

(1) Gao, J.; Truhlar, D. G.; Wang, Y.; Mazack, M. J. M.; Löffler, P.; Provorse, M. R.; Rehak, P. *Acc. Chem. Res.* **2014**, *47*, 2837−2845.

(2) Giese, T. J.; Huang, M.; Chen, H.; York, D. M. *Acc. Chem. Res.* **2014**, *47*, 2812−2820.

(3) Han, J.; Truhlar, D. G.; Gao, J. *Theor. Chem. Acc.* **2012**, *131*, 1161−1161.

(4) Han, J.; Mazack, M. J. M.; Zhang, P.; Truhlar, D. G.; Gao, J. *J. Chem. Phys.* **2013**, *139*, 054503.

(5) Giese, T. J.; Chen, H.; Dissanayake, T.; Giambaşu, G. M.; Heldenbrand, H.; Huang, M.; Kuechler, E. R.; Lee, T.-S.; Panteva, M. T.; Radak, B. K.; York, D. M. *J. Chem. Theory Comput.* **2013**, *9*, 1417−1427.

(6) Zhang, P.; Truhlar, D. G.; Gao, J. *Phys. Chem. Chem. Phys.* **2012**, *14*, 7821−7829.

(7) Giese, T. J.; Panteva, M. T.; Chen, H.; York, D. M. *J. Chem. Theory Comput.*, DOI: 10.1021/ct5007983.

(8) Giese, T. J.; Chen, H.; Huang, M.; York, D. M. *J. Chem. Theory Comput.* **2014**, *10*, 1086−1098.

(9) Kapustin, E. A.; Minkov, V. S.; Stare, J.; Boldyreva, E. V. *Cryst. Growth Des.* **2014**, *14*, 1851−1864.

(10) Wang, J.; Wolf, R. M.; Caldwell, J.; Kollman, P. A.; Case, D. A. *J. Comput. Chem.* **2004**, *25*, 1157−1174.

(11) Song, L.; Han, J.; lin Lin, Y.; Xie, W.; Gao, J. *J. Phys. Chem. A* **2009**, *113*, 11656−11664.

(12) Xie, W.; Orozco, M.; Truhlar, D. G.; Gao, J. *J. Chem. Theory Comput.* **2009**, *5*, 459−467.

(13) Xie, W.; Song, L.; Truhlar, D. G.; Gao, J. *J. Chem. Phys.* **2008**, *128*, 234108.

(14) Xie, W.; Gao, J. *J. Chem. Theory. Comput.* **2007**, *3*, 1890−1900.

(15) Gao, J. *J. Phys. Chem. B* **1997**, *101*, 657−663.

(16) Gao, J.; Wang, Y. *J. Chem. Phys.* **2012**, *136*, 071101.

(17) Cembran, A.; Bao, P.; Wang, Y.; Song, L.; Truhlar, D. G.; Gao, J. *J. Chem. Theory Comput.* **2010**, *6*, 2469−2476.

(18) Jacobson, L. D.; Herbert, J. M. *J. Chem. Phys.* **2011**, *134*, 094118.

(19) Gao, J.; Cembran, A.; Mo, Y. *J. Chem. Theory Comput.* **2010**, *6*, 2402−2410.

(20) Gaus, M.; Goez, A.; Elstner, M. *J. Chem. Theory Comput.* **2013**, *9*, 338−354.

(21) Giese, T. J.; Huang, M.; Chen, H.; York, D. M. *Acc. Chem. Res.* **2014**, *47*, 2812−20.

(22) Jorgensen, W. L.; Chandrasekhar, J.; Madura, J. D.; Impey, R. W.; Klein, M. L. *J. Chem. Phys.* **1983**, *79*, 926−935.

(23) Horn, H. W.; Swope, W. C.; Pitera, J. W.; Madura, J. D.; Dick, T. J.; Hura, G. L.; Head-Gordon, T. *J. Chem. Phys.* **2004**, *120*, 9665−9678.

(24) Temelso, B.; Archer, K. A.; Shields, G. C. *J. Phys. Chem. A* **2011**, *115*, 12034−12046.

(25) Case, D. A.; Babin, V.; Berryman, J. T.; Betz, R. M.; Cai, Q.; Cerutti, D. S.; Cheatham, III, T. E.; Darden, T. A.; Duke, R. E.; Gohlke, H.; Goetz, A. W.; Gusarov, S.; Homeyer, N.; Janowski, P.; Kaus, J.; Kolossváry, I.; Kovalenko, A.; Lee, T. S.; LeGrand, S.; Luchko, T.; Luo, R.; Madej, B.; Merz, K. M.; Paesani, F.; Roe, D. R.; Roitberg, A.; Sagui, C.; Salomon-Ferrer, R.; Seabra, G.; Simmerling, C. L.; Smith, W.; Swails, J.; Walker, R. C.; Wang, J.; Wolf, R. M.; Wu, X.; Kollman, P. A. *AMBER 14*; University of California: San Francisco, CA, 2014.

(26) Andersen, H. C. *J. Chem. Phys.* **1980**, *72*, 2384−2393.

(27) Darden, T.; York, D.; Pedersen, L. *J. Chem. Phys.* **1993**, *98*, 10089−10092.

(28) Essmann, U.; Perera, L.; Berkowitz, M. L.; Darden, T.; Hsing, L.; Pedersen, L. G. *J. Chem. Phys.* **1995**, *103*, 8577−8593.

(29) Miyamoto, S.; Kollman, P. A. *J. Comput. Chem.* **1992**, *13*, 952−962.

(30) Ryckaert, J. P.; Ciccotti, G.; Berendsen, H. J. C. *J. Comput. Phys.* **1977**, *23*, 327−341.

(31) Frenkel, D.; Smit, B. *Understanding Molecular Simulation*; Academic Press: San Diego, CA, 1996.

(32) Basconi, J. E.; Shirts, M. R. *J. Chem. Theory Comput.* **2013**, *9*, 2887−2899.

(33) Shirts, M. R. *J. Chem. Theory Comput.* **2013**, *9*, 909−926.

(34) Berendsen, H. J. C.; Postma, J. P. M.; van Gunsteren, W. F.; Dinola, A.; Haak, J. R. *J. Chem. Phys.* **1984**, *81*, 3684−3690.

(35) Dünweg, B.; Kremer, K. *J. Chem. Phys.* **1993**, *99*, 6983−6997.

(36) Yeh, I.-C.; Hummer, G. *J. Phys. Chem. B* **2004**, *108*, 15873−15879.

(37) Vega, C.; Sanz, E.; Abascal, J. L. F. *J. Chem. Phys.* **2005**, *122*, 114507.

(38) Lee, T.-S.; Radak, B. K.; Huang, M.; Wong, K.-Y.; York, D. M. *J. Chem. Theory Comput.* **2014**, *10*, 24−34.

(39) Frauenheim, T.; Seifert, G.; Elstner, M.; Hajnal, Z.; Jungnickel, G.; Porezag, D.; Suhai, S.; Scholz, R. *Phys. Status Solidi B* **2000**, *217*, 41−62.

(40) Elstner, M.; Frauenheim, T.; Kaxiras, E.; Seifert, G.; Suhai, S. *Phys. Status Solidi B* **2000**, *217*, 357−376.

(41) Elstner, M.; Porezag, D.; Jungnickel, G.; Elsner, J.; Haugk, M.; Frauenheim, T.; Suhai, S.; Seifert, G. *Phys. Rev. B* **1998**, *58*, 7260−7268.

(42) Nam, K.; Cui, Q.; Gao, J.; York, D. M. *J. Chem. Theory Comput.* **2007**, *3*, 486−504.

(43) Gaus, M.; Lu, X.; Elstner, M.; Cui, Q. *J. Chem. Theory Comput.* **2014**, *10*, 1518−1537.

(44) Wang, L.-P.; Chen, J.; Voorhis, T. V. *J. Chem. Theory Comput.* **2013**, *9*, 452−460.

(45) Wang, L.-P.; Head-Gordon, T.; Ponder, J. W.; Ren, P.; Chodera, J. D.; Eastman, P. K.; Martinez, T. J.; Pande, V. S. *J. Phys. Chem. B* **2013**, *117*, 9956−9972.

(46) Burger, S. K.; Cisneros, G. A. *J. Comput. Chem.* **2013**, *37*, 2313−2319.

(47) Grimme, S. *J. Chem. Theory Comput.* **2014**, *10*, 4497−4514.

(48) Hopkins, C. W.; Roitberg, A. E. *J. Chem. Inf. Model.* **2014**, *54*, 1978−1986.

(49) Vanommeslaeghe, K.; Raman, E. P.; MacKerell, A. D. *J. Chem. Inf. Model.* **2012**, *52*, 3155−3168.

(50) Abascal, J. L. F.; Sanz, E.; Fernández, R. G.; Vega, C. *J. Chem. Phys.* **2005**, *122*, 234511.

(51) Feistel, R.; Wagner, W. *J. Phys. Chem. Ref. Data* **2006**, *35*, 1021−1047.

(52) Parrinello, M.; Rahman, A. *J. Chem. Phys.* **1984**, *80*, 860.

(53) Whalley, E. *J. Chem. Phys.* **1984**, *81*, 4087−4092.

(54) Paesani, F. *Phys. Chem. Chem. Phys.* **2011**, *13*, 19865.

(55) Paesani, F.; Zhang, W.; Case, D. A.; Cheatham, T. E., III; Voth, G. A. *J. Chem. Phys.* **2006**, *125*, 184507.

(56) Paesani, F.; Iuchi, S.; Voth, G. A. *J. Chem. Phys.* **2007**, *127*, 074506.

(57) Medders, G. R.; Babin, V.; Paesani, F. *J. Chem. Theory Comput.* **2014**, *10*, 2906−2910.

(58) Goetz, A. W.; Williamson, M. J.; Xu, D.; Poole, D.; Le Grand, S.; Walker, R. C. *J. Chem. Theory Comput.* **2012**, *8*, 1542−1555.

(59) Le Grand, S.; Goetz, A. W.; Walker, R. C. *Comput. Phys. Commun.* **2013**, *184*, 374−380.

(60) Salomon-Ferrer, R.; Goetz, A. W.; Poole, D.; Le Grand, S.; Walker, R. C. *J. Chem. Theory Comput.* **2013**, *9*, 3878−3888.

(61) Gao, J.; Zhang, J. Z. H.; Houk, K. N. *Acc. Chem. Res.* **2014**, *47*, 2711−2711.

(62) Hengge, A. C. *Acc. Chem. Res.* **2002**, *35*, 105−112.

(63) Huang, M.; York, D. M. *Phys. Chem. Chem. Phys.* **2014**, *16*, 15846−15855.

(64) Chen, H.; Giese, T. J.; Huang, M.; Wong, K.-Y.; Harris, M. E.; York, D. M. *Chem.—Eur. J.* **2014**, *20*, 14336−14343.

(65) Kirby, A. J.; Jencks, W. P. *J. Am. Chem. Soc.* **1965**, *87*, 3209−3216.

(66) Tomasi, J.; Mennucci, B.; Cammi, R. *Chem. Rev.* **2005**, *105*, 2999−3093.

(67) Scalmani, G.; Frisch, M. J. *J. Chem. Phys.* **2010**, *132*, 114110−114124.

(68) Barone, V.; Cossi, M.; Tomasi, J. *J. Chem. Phys.* **1997**, *107*, 3210−3221.

(69) Moser, A.; Range, K.; York, D. M. *J. Phys. Chem. B* **2010**, *114*, 13911−13921.

(70) Zhang, L.; Xie, D.; Xu, D.; Guo, H. *Chem. Commun.* **2007**, *16*, 1638−1640.

(71) Gaus, M.; Cui, Q.; Elstner, M. *J. Chem. Theory Comput.* **2011**, *7*, 931−948.

(72) Haleblian, J.; McCrone, W. *J. Pharm. Sci.* **1969**, *58*, 911−929.

(73) Borka, L.; Haleblian, J. *Acta Pharm. Jugosl.* **1990**, *40*, 71−94.

(74) Vishweshwar, P.; McMahon, J. A.; Bis, J. A.; Zaworotko, M. J. *J. Pharm. Sci.* **2006**, *95*, 499−516.

(75) Brittain, H. G. *Polymorphism in Pharmaceutical Solids*, Vol. *192*; Informa Healthcare: New York, 2009.

(76) Schnieders, M. J.; Fenn, T. D.; Pande, V. S. *J. Chem. Theory Comput.* **2011**, *7*, 1141−1156.

(77) Schnieders, M. J.; Baltrusaitis, J.; Shi, Y.; Chattree, G.; Zheng, L.; Yang, W.; Ren, P. *J. Chem. Theory Comput.* **2012**, *8*, 1721−1736.

(78) Park, J.; Nessler, I.; McClain, B.; Macikenus, D.; Baltrusaitis, J.; Schnieders, M. J. *J. Chem. Theory Comput.* **2014**, *10*, 2781−2791.

(79) Kell, G. S. *J. Chem. Eng. Data* **1975**, *20*, 97−105.

(80) Wagner, W.; Pruß, A. *J. Phys. Chem. Ref. Data* **2002**, *31*, 387−535.

(81) Mills, R. *J. Phys. Chem.* **1973**, *77*, 685−688.

(82) Fernández, D. P.; Mulev, Y.; Goodwin, A. R. H.; Levelt Sengers, J. M. H. *J. Phys. Chem. Ref. Data* **1995**, *24*, 33−70.

(83) Soper, A. K. *ISRN Phys. Chem.* **2013**, *2013*, 279463.

(84) Skinner, L. B.; Huang, C.; Schlesinger, D.; Pettersson, L. G. M.; Nilsson, A.; Benmore, C. J. *J. Chem. Phys.* **2013**, *138*, 074506.

(85) Soper, A. K.; Phillips, M. G. *Chem. Phys.* **1986**, *107*, 47−60.